ISSN 1063-7788, Physics of Atomic Nuclei, 2022, Vol. 85, No. 6, pp. 785–801. © Pleiades Publishing, Ltd., 2022.

NUCLEI
Experiment

Investigation of Excited States of the ^{13}C Nucleus in Alpha-Particle Scattering

S. A. Goncharov[1], A. S. Demyanova[2]*, A. N. Danilov[2], V. I. Starastsin[2,3], T. L. Belyaeva[4], W. Trzaska[5], N. Burtebayev[6,7], M. Nasurlla[6,7], and Yu. B. Gurov[3,8]

Received September 13, 2022; revised September 13, 2022; accepted September 15, 2022

Abstract—A theoretical analysis of available experimental data on elastic and inelastic $\alpha+^{13}$C scattering in the energy region extending up to 90 MeV is performed. The parameters of a semimicroscopic potential are found on the basis of the dispersive optical model. The potentials found in this way are used in analyzing, by the distorted-wave Born approximation, data that the authors recently measured for inelastic scattering at energies of 65 and 90 MeV. Experimental data for the states at 3.68 and 7.55 MeV are presented for the first time. These states are considered under the assumption that, within the standard rotational model, they are members of the ground-state rotational band. A satisfactory description of angular distributions is obtained, and deformation lengths are determined. A model phenomenological form factor is used for the remaining excitations in the energy range extending up to 11 MeV. The present analysis confirms the presence of a neutron halo in the 3.09-MeV state. A similarity of form of the inelastic form factors obtained for the 8.86-, 10.996-, and 11.08 MeV states and the proximity of their radii gives grounds to assume that the ^{13}C nucleus in these three states has an enhanced size and similar structures. A comparison of the radial dependences of the form factors for the 9.90- and 8.86-MeV states shows that the wave function for the 9.90-MeV state has a substantially smaller spatial extension. These results agree with the values obtained for the radii of the states under discussion on the basis of the modified diffraction model.

DOI: 10.1134/S1063778823010210

1. INTRODUCTION

The ^{13}C nucleus is a good example of a "normal" nucleus that is well described by the shell model. Negative-parity states are determined by various configurations of nine nucleons in the p shell. Positive-parity states with a nucleon in the *sd* shell are well described by its coupling to the ground state and the first excited state of the ^{12}C nucleus. Some alpha-cluster states appear at higher excitation energies in the region of respective thresholds. Thus, the scheme of ^{13}C levels has been determined reliably up to excitation energies of about 10 MeV and is described in detail in [1].

However, some new ideas and results revived interest in the ^{13}C nucleus. The hypothesis that an alpha-particle Bose–Einstein condensate (αBEC) may exist in light nuclei [2, 3] is the most ambitious. It is expected that respective nuclear states are dilute systems of nearly noninteracting alpha particles having zero momentum of relative motion and lying near thresholds for breakup to alpha particles— $A \to n\alpha$. Some properties of such condensate structures were predicted in [2, 3] and were observed experimentally in [4–6] in the second excited state $^{12}CO_2^+$ at $E^* = 7.65$ MeV—a so-called Hoyle state. It is expected [7–10] that analogs of the Hoyle state will manifest themselves in some neighboring nuclei—for example, in ^{13}C. In this case, it is expected that a valence neutron is coupled to the core that is the Hoyle state. The respective states having spin–parities of $1/2^-$ and $1/2^+$ and lying near the $^{12}C(0_2^+) + n$ threshold (12.60 MeV) may display features characteristic of this cluster configuration. An enhanced size of the nucleus in these states is the most distinct indication that such an exotic structure does indeed exist.

[1]Moscow State University, Moscow, Russia.
[2]National Research Centre Kurchatov Institute, Moscow, Russia.
[3]National Research Nuclear University MEPhI, Moscow, Russia.
[4]Universidad Autónoma del Estado de México, Toluca, México.
[5]JYFL, Department of Physics, University of Jyväskylä, Jyväskylä, Finland.
[6]Institute of Nuclear Physics, National Nuclear Center of Republic of Kazakhstan, Almaty, Republic of Kazakhstan.
[7]Al-Farabi Kazakh National University, Almaty, Republic of Kazakhstan.
[8]Joint Institute for Nuclear Researches, Dubna, Russia.
*E-mail: a.s.demyanova@bk.ru

Yamada and Funaki [9, 10] predicted that, in the $1/2_2^-$, $1/2_3^-$, and $1/2_4^-$ states, the root-mean-square radii exceed the ground-state root-mean-square radius by 0.6 to 0.8 fm. Kabawata and his colleagues [7, 8] observed strong monopole transitions occurring in inelastic $^{13}C + \alpha$ scattering and leading to the above $1/2^-$ states at the energies of $E_x = 8.86$, 11.08, and 12.5 MeV, respectively. Two dilute cluster states whose quantum numbers are $1/2_2^+$ and $1/2_3^+$ and which have the radii of $R_{\rm rms} = 4.0$ and 5.40 fm, respectively, were additionally predicted in [9, 10] near the $3\alpha + n$ threshold and can in principle be associated with known states at 11.00 and 12.14 MeV. It is expected that the latter will show distinct signatures of alpha-particle condensation. In one of their recent studies [11], Yamada and Funaki assumed that the configuration of the $1/2^-$ states does not feature a dominant $^{12}C(\text{Hoyle}) + n$ component but is closer to the $^9Be + \alpha$ configuration. The same applies to $1/2_2^+$, $1/2_3^+$, and $1/2_4^+$ states. Only the $1/2_5^+$ state, which have not yet been observed experimentally and which, according to calculations, is expected to be around 15 MeV, can be viewed as an alpha-condensate state [11]. Calculations predict an enormous radius of about 4 fm in this state and a probability of about 52% for the $(0S)_\alpha^3(S)_n$ condensate configuration.

Similar searches for possible analogs of the Hoyle state were performed within the method of antisymmetrized molecular dynamics (AMD) [12]. The internal structure of $1/2^-$ and $1/2^+$ excited states was considered. It was shown that the $^9Be + \alpha$ structure was peculiar to the $1/2_2^-$ and $1/2_3^+$ states, which form a doublet. According to predictions of the AMD method, the $1/2_3^-$, $1/2_4^-$, and $1/2_5^-$ states have a $3\alpha + n$ configuration but they cannot be analogs of the Hoyle state because of the mixing of the $^{12}C(0_2^+)0p_{1/2}$ and $^{12}C(0_2^+)0p_{3/2}$ configurations and because of the smallness of the S factor in the former. According to the opinion proposed by the authors of [12], the absence of analogs of the Hoyle state in that case is due to a strong $\alpha - n$ interaction in the P wave. The $1/2_2^+$ state lying, according to calculations, at around 15.4 MeV and having a condensate-configuration probability of 64% was viewed as a possible analog of the Hoyle state. The respective experimental state lies at about 11 MeV. We hope that this state can be obtained experimentally.

Alpha-particle clustering in excited states of the ^{13}C nucleus was also analyzed from a different point of view. Milin and von Oertzen [13] assumed the existence of two rotational bands built on the $3/2_2^-$ state at 9.90 MeV and an not-yet-discovered $3/2^+$ state. These states were considered as a parity doublet of the $^9Be(\text{g.s.}) + \alpha$ cluster structure. Furutachi and Kimura [14] proposed two $K^\pi = 3/2^-$ rotational bands with a large moment of inertia near the $3\alpha + n$ threshold (12.2 MeV). One of these bands is expected to have a linear 3α configuration (see also [15]) and can be identified with the band based on the 9.90-MeV state. In [14], it is predicted that the radii in the states that are members of this band are enhanced ($R_{\rm rms} \sim 3.2$–3.3 fm).

The spectrum of the ^{13}C nucleus may also involve dilute states of a different type. Soon after the discovery of a neutron halo in the ground states of some nuclei in the vicinity of the neutron drip line, it was assumed [16] that similar structures might also be discovered in excited states. The $1/2^+$ state at 3.09 MeV in ^{13}C was indicated as the most probable candidate, and some pieces of experimental evidence of the existence of a halo in this state were obtained in [17,18] on the basis of an analysis of the reaction $^{12}C(d,p)^{13}C$.

Our group also studied actively states of the ^{13}C nucleus within the Modified Diffraction Model (MDM) that we developed [19]. The first application of the MDM method [20] to available experimental data on alpha-particle and ^3He scattering on ^{13}C, which are rather scanty, showed that the $1/2_1^+$ state at 3.09 MeV and the $1/2_2^-$ state at 8.86 MeV do indeed have enhanced radii. For want of experimental data, it was necessary to perform our own experiments aimed at studying alpha-particle scattering on ^{13}C at 65 and 90 MeV [21–23]. Both experiments were performed by employing at the K130 cyclotron of University of Jyväskylä (Finland) with the use of a large scattering chamber. These new experimental data made it possible to conclude with confidence that low-lying states of the ^{13}C nucleus feature structures of several types. The $1/2_1^+$ first excited state at 3.09 MeV is a state with a neutron halo [21, 22]. The $1/2_2^-$ state at 8.86 MeV and the $1/2_3^-$ state at 11.08 MeV are alpha-cluster states characterized by enhanced radii—they are possible analogs of the Hoyle state [21, 22, 24]. The values obtained for the radii of these states agree within the errors with the radius of the Hoyle state [19].

The result obtained for the $3/2_2^-$ state at 9.90 MeV is quite unexpected. It turned out that it was a compact state of radius that is smaller than the ground-state radius by about 10% [21–23]. At the same time, a dilute structure was predicted in [14] with an enhanced radius more than 3 fm. In [13, 14], it is assumed that this state has a rotational structure and that the formation of a rotational band on its basis is possible. The internal structure of the state

in question was considered in [25], and it was shown that this state had a $^9\mathrm{Be}(3/2_1^-) + \alpha$ cluster structure. A reduced radius obtained for it by the MDM method is compatible with this. We have also considered the isobaric analog state in ^{13}N at 9.48 MeV [24] and obtained, within the MDM framework, a radius that agrees within the errors with the ground-state radius. However, a rather large error in this result should be noted. Therefore, it is necessary to perform additional studies of this issue.

It is noteworthy that, in considering excited states of the ^{13}C nucleus, we did not found any signatures of rotational bands. In [26], it was assumed that a rotational band could be built on the Hoyle state. This brings about the reasonable question of whether rotational bands built on analogs of the Hoyle state in the ^{13}C nucleus exist. On the basis of the new type of symmetry D'_{3h} a rotational nature was predicted in [27] for a whole group of low-lying states of the ^{13}C nucleus. A similar symmetry type of D_{3h} was predicted earlier in [26] for the ^{12}C nucleus. Six rotational band were proposed in [27] for the ^{13}C nucleus; that is, almost all of the low-lying states of ^{13}C were distributed among the bands. In the case of confirmation of this hypothesis, our concepts of the structure of ^{13}C will change drastically.

Thus, we have seen that, despite the opulence of both experimental and theoretical studies devoted to ^{13}C, there remain open questions concerning the internal structure of some states. This served as a motivation for us to perform a thorough theoretical analysis of existing experimental data. In this article, we present the results obtained by analyzing, in the distorted-wave Born approximation (DWBA) our experimental data on alpha-particle scattering on ^{13}C at the energies of 65 and 90 MeV [21–24]. The calculations by the DWBA method were performed using the FRESCO [28] and DWUCK4 [29] codes.

2. EXPERIMENT

The experiments were conducted at two energy values of 65 MeV [21] and 90 MeV [22, 23] at the K130 cyclotron of University of Jyväskylä (Finland) with the use of a large scattering chamber. Self-supported ^{13}C films 0.3 mg/cm^2 thick were used as targets, where the impurities were exhausted by the presence of ^{12}C and ^{16}O only in a total amount not exceeding 2%. These impurities did not have a substantial effect on ^{13}C states. In order to obtain the required resolution of 200 to 250 keV, the monochromatization of the beam used was performed before the experiment. This made it possible to reduce the spreading of the beam by a factor of two to three. The scattered alpha particles were detected by means of the standard ΔE–E procedure. Thin detectors 100, 250 and 380 μm thick were used as ΔE detectors. All E detectors were 3.6 mm thick. Simultaneously, four telescopes were used positioned at different angles in the reaction plane. The telescope was moved after each series of measurements, with the result that the total measured angular range was 5° to 72° in the laboratory frame for the experiment at 65 MeV and 6° to 40° for the experiment at 90 MeV. Files of sequential events were accumulated in the course of the experiment, and these files were processed in an off-line mode.

The experimental spectra cover the energy range extending to an excitation energy of about 12 MeV. Typical spectra of both experiments are given in Fig. 1. The background in the figures is represented by a dashed line. Basically, this background is physical and admits a description in terms of the $^{12}\mathrm{C} + n + \alpha$ and $^9\mathrm{Be} + \alpha + \alpha$ phase spaces represented by the dashed line in Fig. 1. Angular distributions were obtained for elastic scattering [21–23] and for excited states at 3.09 MeV [21, 22, 24]; 3.68, 7.55, and 8.86 MeV [21, 22, 24]; 9.90 MeV [21–24]; and 11.08 MeV [24]. Data on the angular distributions for the 3.68- and 7.55-MeV states are presented here for the first time. The angular distributions obtained in the experiments under discussion were analyzed using the FRESCO [28] and DWUCK4 [29] codes.

3. THEORETICAL ANALYSIS OF DATA

In order to analyze data on inelastic scattering, we apply the DWBA method. The use of this method requires knowing optical potentials that describe elastic scattering in the entrance and exit reaction channels.

3.1. Optical Potential Model

In order to describe elastic scattering in nucleus–nucleus collisions at energies in the range extending to 100 MeV per nucleon, a SemiMicroscopic (SM) model was developed in [30] within the Dispersive Optical Model (DOM) for optical potentials (SMDOM). Later on, the SMDOM approach, which is theoretically based on the effective-potential formalism [31], was tested many times.

Within the SMDOM framework, the optical potential is represented in the form

$$V(r,E) = V_{\mathrm{Coul}}(r) + V_F(r,E) + V_P(r,E) + iW(r,E) + V_{\mathrm{so}}(r), \quad (1)$$

where $V_{\mathrm{Coul}}(r)$ is the Coulomb potential of a uniformly charged sphere whose radius R_{C} is estimated by employing the root-mean-square radii of colliding nuclei. The second term in expression (1) is

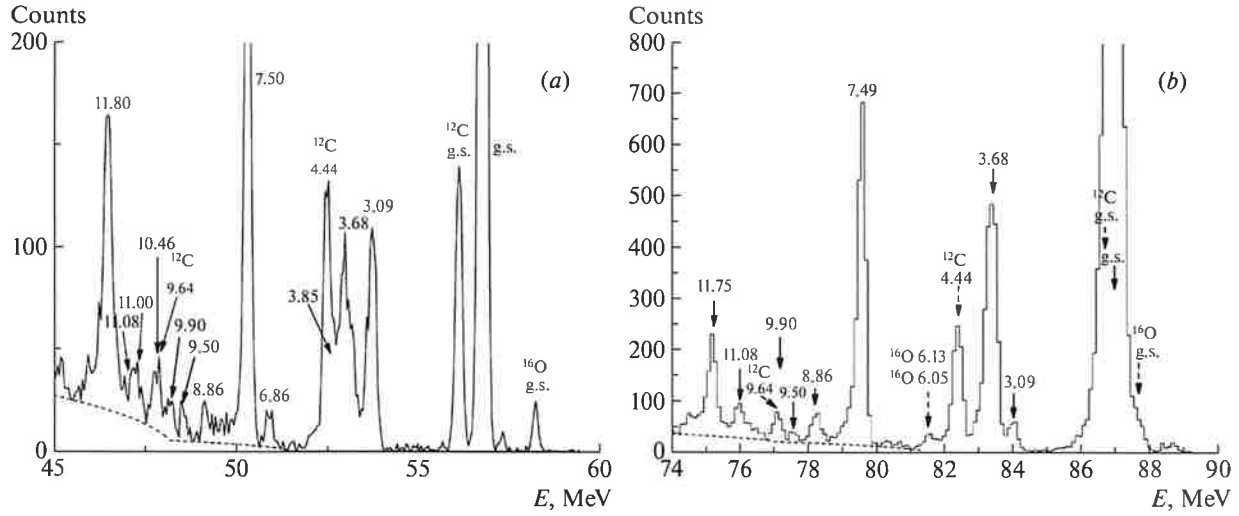

Fig. 1. Typical experimental spectra: (*a*) typical spectrum at an angle of 38.5° in the experiment at the energy of 65 MeV and (*b*) typical spectrum at an angle of 20° in the experiment at the energy of 90 MeV. For either spectrum, the background is represented by the dashed line.

the mean-field potential calculated microscopically on the basis of the double-folding model (see below).

The third and fourth terms represent the dynamical polarization potential constructed phenomenologically on the basis of of a combination of the volume and surface Woods–Saxon forms. Its imaginary (absorbing) part has the form

$$iW = -iW_S(E)\,f(x_S) + i4W_D(E)\,\frac{df(x_D)}{dx_D}, \quad (2)$$

where $f(x) = (e^x + 1)^{-1}$, $x_{S(D)} = (r - R_{S(D)})/a_{S(D)}$, and $R_{S(D)} = r_{S(D)}(A_p^{1/3} + A_t^{1/3})$.

The geometric parameters (radii and diffuseness parameters of Woods–Saxon forms) are assumed to be energy-independent. This permits taking explicitly into account dispersion relations and representing the real part of the dynamical polarization potential (dispersion correction) in the form

$$V_P(r, E) = V_S(E)\,f(x_S) + V_D(E)\,\frac{df(x_D)}{dx_D}. \quad (3)$$

The parameter of the dynamical polarization potential are determined from a simultaneous analysis of all available sets of data at different energies. Four strength parameters (V_S, V_D, W_S, and W_D) are determined at each energy value, whereas four geometric parameters (r_S, a_S, r_D, and a_D) are assumed to have the same values at all energies.

Expression (1) also includes a standard phenomenological spin–orbit potential $V_{so}(r)$ (in target spin) in the form of the derivative of the Woods–Saxon form. This term permits improving the description of data at large angles.

This model, which employs dispersion relations, effectively involves a smaller number of adjustable parameters than the usual phenomenological optical model, where one determines the whole parameter set at each energy value. This makes it possible to reduce ambiguities in the analysis.

3.2. Calculation of the Mean-Field Potential

A microscopic calculation of the mean-field potential on the basis of the double-folding method with allowance for the exchange component (which arises as a consequence of the Pauli exclusion principle) became widespread. The approximation of single-nucleon knockout exchange (SNKE) is used for the exchange component (see, for example, [30, 32] and references therein). A method for correcting the exchange component in terms of its energy-dependent renormalization determined empirically was proposed and tested in [33, 34]. Although this method implies a two-step analysis, it permits taking effectively into account multiparticle exchange via correcting the energy dependence of the exchange component. A simple approximation for nuclear density matrices in calculating the exchange component was proposed in the same studies. This approximation, which simplifies the calculations substantially, yields a result that is close to that in the harmonic-oscillator model, but which shows a more correct asymptotic behavior. A more appropriate approximation for calculating density matrices was recently proposed and tested in [35]. This approximation leads to results that are closer to those in the harmonic-oscillator model at small radii as well.

In the present study, we apply this microscopic-calculation version, which is the most recent one. In the SNKE approximation, the mean-field potential for the interaction of nucleus a with nucleus A can be expressed (see, for example, [30]) in terms of the convolution integrals for the direct and exchange components (spin variables and spin components being omitted) as

$$\hat{V}_F = \hat{V}^D + \hat{V}^E. \quad (4)$$

Here, the potentials are treated as matrices in which the diagonal terms are optical potentials that determine elastic scattering in the channel being considered, while off-diagonal terms are transition potentials that are responsible for inelastic excitations.

The direct component has the form

$$\hat{V}^D(r) = \sum_{T=0,1} \hat{V}_T^D(r), \quad (5)$$

$$\hat{V}_T^D(r) = \int dr_1 dr_2 g_T^{c,D}(s)\, \rho_T^a(r_1)\, \rho_T^A(r_2),$$

where $\rho_T^{a,A}$ stands for the scalar ($T=0$) and isovector ($T=1$) components of nuclear densities (transition densities for off-diagonal elements), $s = r_1 - r_2 + r$ is the radius vector between individual nucleons of individual nuclei, and r is the distance between the centers of mass of the nuclei.

The localized exchange component has the form

$$\hat{V}^E(r,E) = \sum_{T=0,1} \hat{V}_T^E(r,E), \quad (6)$$

$$\hat{V}_T^E(r,E) = \int dr_1 dr_2 g_T^{c,E}(s)\, \rho_T^a(r_1, r_1+s)$$

$$\times \rho_T^A(r_2, r_2 - s) \exp\left(\frac{iK(E,r)\, s}{\mu}\right).$$

Here, $\rho_T^i(r_1, r_2)$ are the respective components of the nuclear density matrices (transition density matrices for off-diagonal elements), while the local momentum $K(E,r)$ is given by

$$K^2(E,r) = \frac{2\mu}{\hbar^2}\left(E - V(r) - V_C(r)\right), \quad (7)$$

where $V(r)$ and $V_C(r)$ are the nuclear and Coulomb potentials of interaction between colliding nuclei.

A density dependence in the form of a density-dependent factor modifying the M3Y model interaction is included in the effective nucleon–nucleon interactions (central direct and exchange components in the case being considered); that is,

$$g(s,\rho) = f(\rho)\, g(s), \quad (8)$$

where the indices are omitted. In the present study, use is made of the parametrization

$$f(\rho) = C\left[1 + \alpha e^{-\beta\rho} - \gamma\rho\right] \quad (9)$$

in the CDM3Y6 version, where the parameters are determined on the basis of the properties of cold nuclear matter [36], but, in contrast to that study, an ad hoc energy dependence is not introduced here.

Further, the application of Fourier–Bessel integral transformations leads to expressions for calculating the exchange component. Specifically, we have

$$\hat{V}_T^E(E,r) \quad (10)$$

$$= 4\pi \int_0^\infty g_T^{c,E}(s,\rho)\, j_0(K(E,r)\, s/M)\, s^2 ds$$

$$\times \int f_T^a(r_1, s)\, f_T^A(|r_1 - r|, s)\, dr_1,$$

where $K(E,r)$ is the modulus of the local momentum and the density matrices reduce, after the separation of part of the angular variables, to the so-called density profiles $f_T^i(x,s)$ ($i = a, A$). Taking into account the approximation proposed in [35], we use for them the expression

$$f_T^i(x,s) = \rho_T^i(x)\left[1 - \bar{D}_T^i \frac{s^2}{4b_i^2}\right] \quad (11)$$

$$\times \exp\left(-\frac{s^2}{4b_i^2}\right),$$

where $\rho_T^i(x)$ is an empirical single-particle density (matter density—isoscalar at $T=0$ and isovector at $T=1$) and

$$\bar{D}_T^i = \frac{1}{N + (-1)^T Z} \quad (12)$$

$$\times \left[\frac{N(N-2)}{N+1} + (-1)^T \frac{Z(Z-2)}{Z+1}\right]$$

(in the case of $N = Z$, we assume that the isovector components are absent).

For $A \leqslant 4$ nuclei, use can be made of the approximate formula that we applied earlier in [33] and which corresponds to $\bar{D}_T^i = 0$.

For the harmonic-oscillator parameter, we make use of the systematics from [37]:

$$b_{i,p}^2 = b_{i,n}^2 = b_i^2 = 0.983A^{1/3} + 0.373\ [\text{fm}^2]. \quad (13)$$

For the material alpha-particle density, we employed a Gaussian form, which yields the root-mean-square radius of $R_m = 1.47$ fm. For the ground-state matter density of the ^{13}C nucleus, $\rho_m(r) = \rho_p(r) + \rho_n(r)$, we applied the model of the three-parameter Fermi distribution traditionally normalized to the number of particles. Also, we used the following parameter values:

$$w_p = 0.15\ \text{fm}, \quad c_p = 2.18\ \text{fm}, \quad (14)$$

$$a_p = 0.395 \text{ fm}, \quad w_n = 0.135 \text{ fm},$$
$$c_n = 2.16 \text{ fm}, \quad a_n = 0.395 \text{ fm},$$

It is noteworthy the proton distribution density $\rho_p(r)$ leads values that are close to the experimental values of the charge form factor [38] and the root-mean-square charge radius, $R_{ch} = 2.46$ fm [39]; the root-mean-square matter radius is $R_m = 2.32$ fm.

In order to correct the energy dependence of the exchange component from [33, 34], we introduce an additional normalization factor $\phi(E)$. After that, the corrected exchange component of the mean field,

$$V^E(r, E) = (1 + \phi(E))\, V^{(\text{SNKE})}(r, E), \quad (15)$$

is determined from a comparison of the energy dependence of the volume integral of the mean field calculated with the exchange component in the SNKE approximation,

$$J_F^{(\text{SNKE})} = J^D + J^{(\text{SNKE})}, \quad (16)$$

with the empirical energy dependence of the volume integral $J_{\text{av}}(E)$ of the mean field in the form (17) whose parameters are determined at the first stage of a phenomenological analysis within the dispersive optical model [40],

$$J_{\text{av}}(E) = a + b\exp(-cE); \quad (17)$$

that is,

$$J^{(\text{SNKE})}(E)\phi(E) = J_{\text{av}}(E) - J_F^{(\text{SNKE})}(E). \quad (18)$$

Since the parameters of the density dependence of effective nucleon–nucleon interactions were fitted to the properties of cold nuclear matter in the Hartree–Fock approximation, which is expressed in terms of the same convolution integrals [36], it is natural to set

$$\phi(0) = 0. \quad (19)$$

In order to perform estimations at any energies, it is convenient to approximate $\phi(E)$, for example, by a polynomial.

A more comprehensive account of the two-step procedure of analysis and details of the calculations is given in [33–35].

4. RESULTS AND DISCUSSION

4.1. Results of Analysis of Data on Elastic Scattering

On the basis of the optical-potential model described above (SMDOM), we have performed an analysis of experimental data on the differential cross sections for elastic $\alpha+^{13}$C scattering at the energies of $E_{\text{lab}} = 48.7$ MeV [41], 54.1 MeV [41], 65 MeV [21], and 90 MeV [22, 23]. We have obtained the parameters of the SMDOM potential. At the first stage of a phenomenological dispersive analysis, an empirical energy dependence of the volume integral for the mean-field potential was determined in the form

$$J_{\text{av}}(E) = 309.3 + 50\exp(-0.003E_{\text{cm}}). \quad (20)$$

Apart from a constant, this result coincides with the dependence obtained earlier for the $\alpha+^{12}$C system [6]. The correcting factor $\phi(E)$ was approximated by third-degree polynomial as

$$\phi(E) = 1.115 \times 10^{-3}E_{\text{cm}} - 1.79 \quad (21)$$
$$\times 10^{-6}E_{\text{cm}}^2 + 1.5 \times 10^{-8}E_{\text{cm}}^3.$$

The strength parameters of the dynamical polarization potential that were found at the second step of our analysis are given in в Table 1 along with the volume integrals and calculated reaction cross sections. For all energies, the geometric parameters were fixed at the values

$$r_S = 1.2 \text{ fm}, \quad a_S = 0.50 \text{ fm}, \quad (22)$$
$$r_D = 0.70 \text{ fm}, \quad a_D = 0.40 \text{ fm},$$
$$r_C = 0.7\ fm$$

in determining the radii of the potentials, $R_i = r_i(A_p^{1/3} + A_t^{1/3})$ $(i = S, D, C, \text{so})$. Table 1 also gives the parameter values evaluated at the energies corresponding to the exit channels of inelastic scattering that lead to the excited states being studied.

A standard phenomenological spin–orbit potential (in target spin) made it possible to improve the description of the data at large angles upon employing the following parameter values:

$$V_{\text{so}} = 5.0 \text{ MeV}, \quad r_{\text{so}} = 0.65 \text{ fm}, \quad (23)$$
$$a_{\text{so}} = 0.8 \text{ fm}.$$

The quality of description of the experimental angular distributions can be seen in Fig. 2. At the present time, there are virtually no data on the reaction cross sections for $\alpha+^{13}$C scattering in the energy range considered here. Nevertheless, a comparison with data available for the $\alpha+^{12}$C system (see Fig. 3) shows that the potential that we constructed yields adequate values. It should be emphasized that the SMDOM optical potential was originally constructed with allowance for dispersion relations for the dynamical polarization potential. If we approximate the energy dependence of the volume integral of the imaginary part by linear straight-line segments on the basis of the empirical values of the imaginary part of the SMDOM potential, then the calculation of the difference dispersion integral [43]

$$J_P(E, E_S) \equiv J_P(E) - J_P(E_S) \quad (24)$$

Table 1. Strength parameters of the dynamical polarization potential, volume integrals, and reaction cross sections

E_{lab}, MeV	$-V_S$, MeV	$-V_D$, MeV	$-W_S$, MeV	$-W_D$, MeV	$-J_V$, MeV fm^3	$-J_W$, MeV fm^3	σ_r, mb
48.7	7.73	−7.98	6.9	7.0	402.0	87.1	964.9
54.1	7.5	−8.95	7.4	7.8	396.1	94.4	958.9
50.469* (1/2$^-$, 11.08)	7.69	−8.38	7.05	7.27	400.1	89.4	962.1
50.579* (1/2$^+$,10.996)	7.68	−8.39	7.07	7.31	400.0	89.7	962.2
52.020* (3/2$^-$, 9.9)	7.62	−8.69	7.19	7.52	398.3	91.5	959.7
53.379* (1/2$^-$, 8.86)	7.55	−8.92	7.3	7.72	396.8	93.2	957.4
55.101* (5/2$^-$, 7.55)	7.46	−9.23	7.45	7.9	394.8	95.1	954.7
59.944* (5/2$^+$, 3.85)	7.13	−9.78	7.82	8.47	389.4	100.4	946.5
60.166* (3/2$^-$, 3.68)	7.11	−9.83	7.85	8.5	389.1	100.8	946.4
60.948* (1/2$^+$, 3.09)	7.05	−9.86	7.90	8.54	388.3	101.6	945.0
65.0	6.67	−10.16	8.2	8.9	383.4	105.4	938.5
75.451* (1/2$^-$, 11.08)	5.05	−10.09	8.68	9.05	367.3	110.4	916.4
77.004* (3/2$^-$, 9.9)	4.8	−9.97	8.75	9.0	365.2	110.9	913.5
78.365* (1/2$^-$, 8.86)	4.54	−9.85	8.8	8.95	363.0	111.2	910.6
80.089* (5/2$^-$, 7.55)	4.2	−9.6	8.85	8.85	360.4	111.3	906.7
85.160* (3/2$^-$, 3.68)	3.03	−8.9	8.93	8.5	351.1	111.1	893.8
85.942* (1/2$^+$, 3.09)	2.85	−8.8	8.94	8.42	349.6	110.8	891.8
90.0	1.8	−8.0	9.0	8.0	341.9	110.1	881.6

* Estimated values at energies corresponding to exit channels of inelastic scattering to the excited states being studied.

$$= \frac{(E-E_S)}{\pi} P \int dE' \frac{J_W(E')}{(E'-E_S)(E'-E)}$$

and addition of this dispersion correction to the volume integral of the mean-field potential yields the volume integral of the total real part of the optical potential. Apart from a constant, the volume integral obtained in this way agrees well with the empirical values deduced from the analysis of experimental data on elastic scattering (see Fig. 4).

In the energy range being considered, the effect of rainbow scattering clearly manifests itself in the experimental differential cross sections. The calculation performed with the above SMDOM potential in the case of the vanishing imaginary part of the dynamical polarization potential and aimed at determining the cross section corresponding to the far-side component of the amplitude shows a broad maximum that is characteristic of rainbow scattering, which is followed by a smooth decrease, and which is preceded by a deep minimum—the main Airy minimum. The positions of this minimum agree well with the regularity found earlier and repeatedly confirmed (see, for example, [34] and references therein), which consists in the linear dependence on the inverse energy, as can be seen in Fig. 5.

The use of rainbow effects also made it possible to reduce the ambiguity in determining the parameters of the optical potential, and a rather smooth energy dependence of this potential in the energy range being considered permitted evaluating the parameters and integral characteristics of the potential at the energies of exit channels of inelastic scattering that are presented in Figs. 3–5.

4.2. Analysis of Data on Inelastic Scattering

The data from [21–23] on $\alpha+^{13}$C scattering at the alpha-particle energies of 65 and 90 MeV that leads to the excitation of the 1/2$^+$ (3.09 MeV), 3/2$^-$ (3.68 MeV), 5/2$^+$ (3.85 MeV), 5/2$^-$ (7.55 MeV), 1/2$^-$ (8.86 MeV), 3/2$^-$ (9.9 MeV), 1/2$^+$ (10.996 MeV), and 1/2$^-$ (11.08 MeV) states were analyzed by the DWBA method by employing the FRESCO [28] and DWUCK4 [29] codes.

4.2.1. Theoretical description of inelastic scattering. The differential cross section is de-

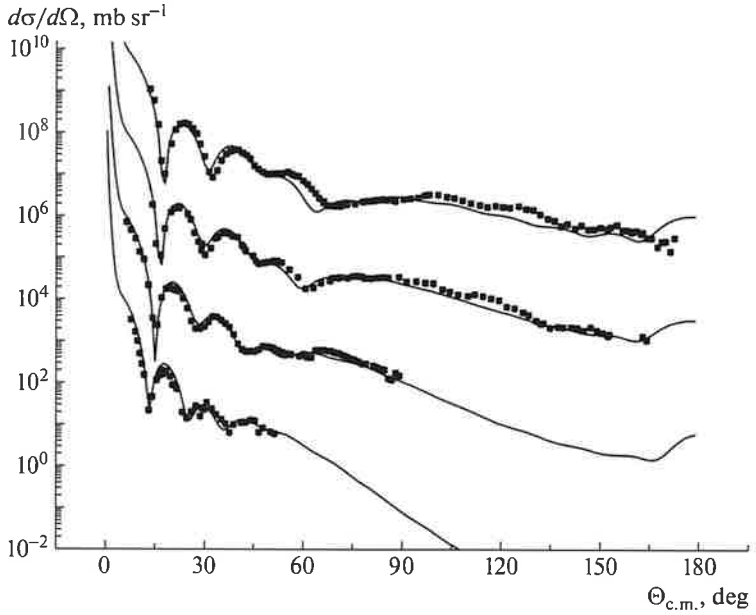

Fig. 2. Differential cross sections for elastic $\alpha+^{13}C$ scattering at the energies of (from bottom to top) 90 MeV [22], 65 MeV [21] (the cross-section values were multiplied by 10^2), 54.1 MeV [41] (the cross-section values were multiplied by 10^4), and 48.7 MeV [41] (the cross-section values were multiplied by 10^6). The solid curves represent the results of the calculations performed with the SMDOM potential.

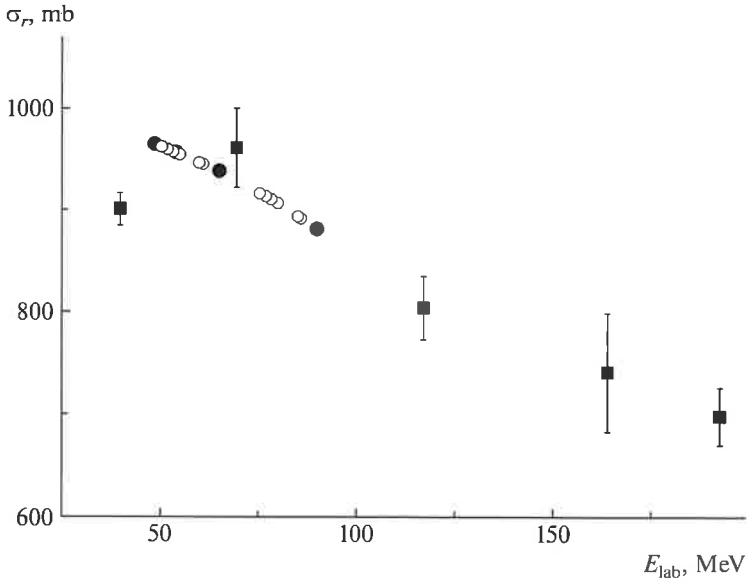

Fig. 3. Cross sections for the $\alpha+^{13}C$ reaction according to (closed circles) calculations with the SMDOM potential, (open circles) calculation with evaluated parameters of the SMDOM potential at the energies of exit inelastic-scattering channels, and (squares) experimental data from [42] for the $\alpha+^{12}C$ system.

termined by the squared modulus of the inelastic-scattering amplitude [31]

$$T_{\alpha'\alpha} = \int u_{\alpha'}^{(-)^*}(K',r) \times \hat{U}_{\alpha'\alpha}(r)\, u_{\alpha}^{(+)}(K,r)\, dr, \quad (25)$$

where $u_{\alpha}^{(+)}$ and $u_{\alpha'}^{(-)}$ are distorted waves—that is, the wave functions for elastic scattering in the entrance and exit channels. In order to calculate the distorted

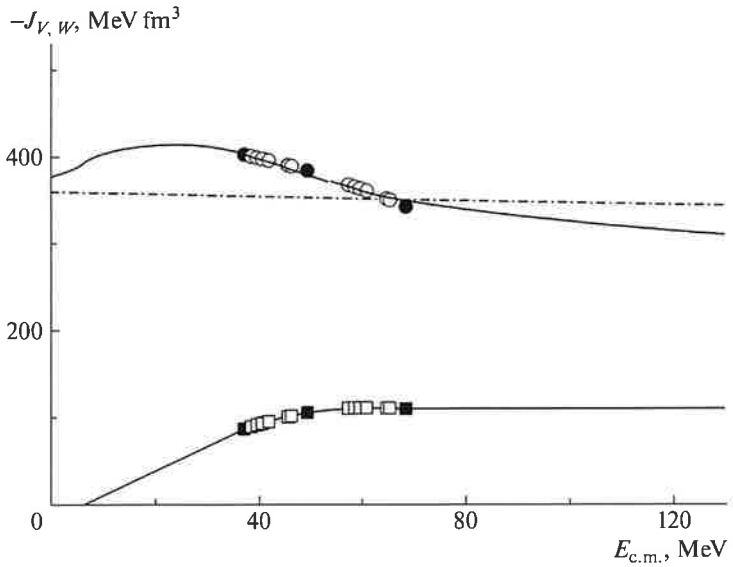

Fig. 4. Volume integrals of the real, J_V (top), and imaginary, J_W (bottom), parts of the optical potential: (closed symbols) calculation with the empirical SMDOM potential and (open symbols) calculations with evaluated parameters of the SMDOM potential at the energies of exit inelastic-scattering channels. The dash-dotted curve represents the volume integral of the mean-field potential (20), the solid curve in the lower part is a linear approximation of J_W, and the solid curve in the upper part stands for the volume integral J_V of the total real part of the optical potential taken to be the sum of the mean field in (20) and the dispersion correction in (24).

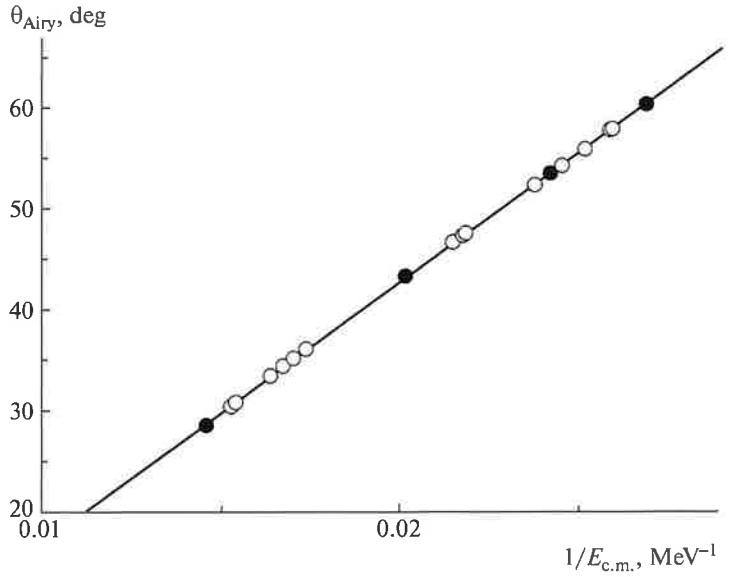

Fig. 5. Positions of first Airy minima: (closed circles) calculation with the empirical SMDOM potential, (solid line) linear approximation, and (closed circles) calculation with the evaluated parameters of the SMDOM potential at the energies of exit inelastic-scattering channels.

waves, we use the strength parameters of the SMDOM potential at respective energy values that was obtained above (see Table 1).

The multipole expansion of the inelastic form factor, which is the matrix element (overlap integral) of inelastic interaction sandwiched between the target-nucleus wave functions in the entrance and exit channels, have a standard form,

$$\hat{U}_{\alpha'\alpha}(\mathbf{r}) = \sum_{LM} F_L(r)\, i^{-L} Y^*_{LM}(\hat{r}), \qquad (26)$$

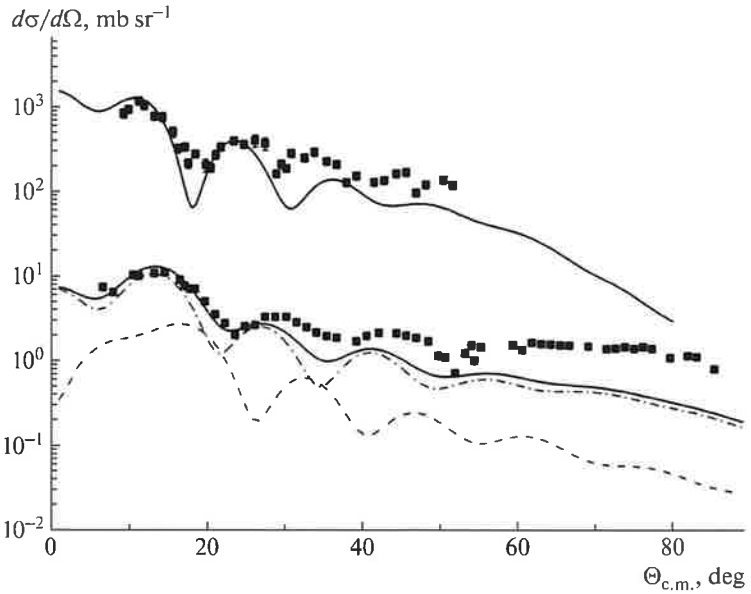

Fig. 6. Differential cross sections for inelastic $\alpha+^{13}C$ scattering at the energies of 65 and 90 MeV (the cross-section values were multiplied by 10^2) that leads to the excitation of the $3/2^-$ state at 3.68 MeV: (points) experimental data and (solid lines) DWBA calculation. For the energy of 65 MeV, the dash-dotted and dashed curves represent the contributions of, respectively, the $3/2^-$ state at 3.68 MeV and the $5/2^+$ state at 3.85 MeV, while the solid curve stands for the sum of these contributions.

where the values of L and M are determined by the rank of inelastic interaction coupling the spins of the nuclei involved and their projections in channels α and α'.

In the problems addressed here, we will apply various phenomenological model forms of the radial inelastic form factors $F_L(r)$.

4.2.2. Analysis of data on inelastic scattering leading to the excitation of the states at 3.68 and 7.55 MeV. In [27], it was assumed that the states at 3.68 and 7.55 MeV are members of the ground-state rotational band ($K^\pi = 1/2^-$). This hypothesis is favored by the proximity of the values obtained within the MDM framework for the radii of these states: 2.3 ± 0.1 fm for the state at 3.68 MeV and 2.3 ± 0.1 fm for the state at 7.55 MeV. These radii agree within the errors with the ground-state radius. In view of this, the radial inelastic form factor $F_L(r)$ is treated within the semimicroscopic rotation-model approach. For a given value of the orbital-angular-momentum transfer L, this approach yields

$$F_L(r) = V_L^F(r,E) + V_L^{\rm DPP}(r,E) + V_L^C(r). \quad (27)$$

In expression (27), the last term V_L^C, which is responsible for Coulomb excitation, is expressed, in a standard way (see, for example, [28, 31]), in terms of the deformation of a uniformly charge sphere; that is,

$$V_L^C(r) = M(EL)e^2(4\pi)^{1/2}(2L+1)^{-1}r^{-L-1}, \quad (28)$$

where the reduced matrix element is expressed in terms of the reduced transition probability as

$$M(EL) = \pm[(I+1)B(EL, I \to I')]^{1/2}. \quad (29)$$

In expression (27), the first term $V_L^F(r,E)$ is the off-diagonal part of the mean-field component of the effective potential [31]. This off-diagonal part is expressed in terms of the transition density in just the same way as in [32]. For it, we employed the empirical rotation-model form [31], which is proportional to the radial derivative of the ground-state matter density; that is,

$$\rho_L^{\rm tr}(r) = -\delta_L^m(4\pi)^{-1/2}d\rho_m/dr, \quad (30)$$

where δ_L^m is the deformation-length parameter.

For transitions within the ground-state rotational band, the dynamical polarization potential (DPP) part of the inelastic form factor, $V_L^{\rm DPP}(r,E)$, is calculated on the basis of the usual rotation model via deforming, with the aid of the respective deformation-length parameters δ_L^P and δ_L^W, the radii of the dynamical polarization potential part of the SMDOM potential [28, 31]; that is,

$$V_L^{\rm DPP}(r,E) = -\delta_L^P(4\pi)^{-1/2}dV_P/dr - i\delta_L^W(4\pi)^{-1/2}dW/dr. \quad (31)$$

The following approximation is usually assumed to be quite accurate:

$$\delta_L^m = \delta_L^P = \delta_L^W = \delta_L. \quad (32)$$

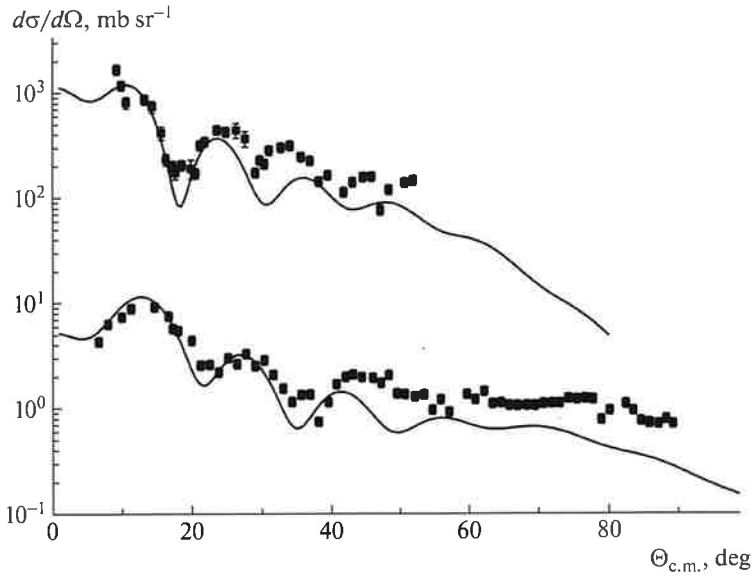

Fig. 7. Differential cross sections for inelastic α+^{13}C scattering at the energies of 65 MeV and 90 MeV (the cross-section values were multiplied by 10^2 in the latter case) that leads to the excitation of the $5/2^-$ state at 7.55 MeV: (points) experimental data and (lines) DWBA calculation.

The parameters δ_L and $M(EL)$ (or $B(EL, I \to I')$) are taken to be adjustable and are found from an analysis of experimental data on differential cross sections.

Figures 6 and 7 show the calculated differential cross sections along with their experimental counterparts for inelastic α+^{13}C scattering at the energies of 65 and 90 MeV that leads to the excitation of the $3/2^-$ state at 3.68 MeV and the $5/2^-$ state at 7.55 MeV. The values obtained for δ_L and $B(EL, I \to I')$ from an analysis are given in Table 2.

It should be noted that, at the energy of 65 MeV, the $3/2^-$ state at 3.68 MeV and the $5/2^+$ state at 3.85 MeV were not separated experimentally. For this reason, the results of the calculations for both of them and their total contribution are shown in Fig. 6. The form-factor model used here for the transition to the $5/2^+$ state at 3.85 MeV is presented below.

In order to estimate the contribution of the excitation of the $5/2^+$ 3.85-MeV state at the laboratory energy of $E_{\rm lab} = 65$ MeV, we assumed that this excitation is a collective one (octupole vibration) and that it is reasonable to approximate the inelastic form factor in just the same way as in Eqs. (27)–(31) by employing the transition density in the form of the first derivative of the ground-state matter density in (30) at the orbital-angular-momentum transfer of $L = 3$. We have obtained the following parameter values: $\delta_3 = 0.82$ fm and $B(E3, 1/2^- \to 5.2^+) = 220e^2$ fm^6.

4.2.3. Analysis of data on inelastic scattering leading to the excitation of the state at 3.09 MeV. We assume that the $1/2^+$ state at 3.09 MeV is a single-particle excited state of the $2s_{1/2}$ valence neutron in the potential of the ^{12}C core in the ground state (with spin $J_c = 0$). The inelastic form factor can then be modeled by means of the so-called microscopic approach to describing inelastic scattering [29]. Here, the radial form factor is determined by the overlap integral of the nucleon–nucleon interaction with single-particle wave functions for the $1p_{1/2}$ valence neutron in the ground state of the ^{13}C target nucleus and the $2s_{1/2}$ valence neutron in the $1/2^+$ excited state of the ^{13}C nucleus at 3.09 MeV. Here, the allowed values of the spin-moment and angular-momentum transfers are $S = 0$ and $J = L = 1$, respectively. We have

$$F_L(r) = 4\pi N\sqrt{2J_i+1} \times \langle j_1' j_2 J_f || Y_L(\hat{r}_1) || j_1 j_2 J_i \rangle \times \int_0^\infty dr_1 r_1^2 R_{l_1' j_1'}(r_1)\, v_L(r, r_1)\, R_{l_1 j_1}(r_1), \quad (33)$$

where $R_{l_1 j_1}(r_1)$ and $R_{l_1' j_1'}(r_1)$ are the normalized (to unity) single-particle neutron radial wave functions for, respectively, the initial (spin J_i) and final (spin J_f) states of the target nucleus, $\langle j_1' j_2 J_f || Y_L(\hat{r}_1) || j_1 j_2 J_i \rangle$ is the reduced matrix element, and $j_2 = J_c$ is the core spin. The normalization factor N carries spectroscopic information about the single-particle states being considered.

Table 2. Deformation lengths and reduced probabilities for transitions in the ground-state rotational band

E_{lab}, MeV	$I^{\pi}(E^*)$ state	L	δ_2, fm	$B(E2, 1/2^- \to I)$, e^2 fm^4
65	$3/2^-$ (3.68 MeV)	2	1.05	13.7
90			1.2	13.7
65	$5/2^-$ (7.55 MeV)	2	1.02	20.5
90			1.02	20.5

For the nucleon–nucleon interaction v, we used the Yukawa potential form containing central (c) and tensor (T) components. In all cases, we employed fixed values for the inverse radius, $\mu_c = 0.707$ fm^{-1} and $\mu_T = 1.139$ fm^{-1}, and for the strength parameters of the Yukawa potential, $v_c = 6.6$ MeV and $v_T = 8.5$ MeV.

The single-particle wave functions for the ground and excited states of the ^{13}C target nucleus were calculated by means of the standard procedure that involves fitting the depth of the well of the Woods–Saxon form V at a fixed value of the neutron separation energy. The geometric parameters for the ground state were fixed at the conventional values of $R = 1.2 \times 12^{1/3} = 2.747$ fm and $a = 0.65$ fm. The geometric parameters for the excited state were taken to be free parameters, along with the normalization factor N. They were fitted in such a way as to describe experimental differential cross sections at least in the region of forward angles, which contains diffraction structures. Originally, the experimental differential cross sections at the energies of 65 and 90 MeV were analyzed by applying, in the exit channel at respective energies, the SMDOM potential (with parameter values from Table 1) featuring the mean-field component calculated by employing the ground-state density of the target nucleus. This resulted in evaluating the parameters of the Woods–Saxon potential, which determines the single-particle wave function for the $2s_{1/2}$ valence neutron in the $1/2^+$ excited state of the ^{13}C nucleus at 3.09 MeV. The results are the following:

$$V = 43.33 \text{ MeV}, \quad R = 2.747 \text{ fm}, \quad a = 1.5 \text{ fm}. \tag{34}$$

The single-particle wave function obtained within this approach for the $s_{1/2}$ valence neutron has a long extension (its root-mean-square radius is $R_n = 6.36$ fm), showing a signature of a neutron halo in the ^{13}C nucleus in the $1/2^+$ state at 3.09 MeV. The evaluation of the root-mean-square radius of the ^{13}C(R_m) nucleus in this state within the model being considered (in just the same way as, for example, in [44]) according to the formula

$$13R_m^2 = 12R_c^2 + 12R_n^2/13 \tag{35}$$

leads to $R_m = 2.8$ fm. A similar value was obtained for the radius within the MDM framework: 2.9 ± 0.2 fm [21, 22]. Here, $R_c = 2.33$ fm is the root-mean-square radius estimated for the ^{12}C core in a standard way (see, for example, [45]) on the basis of the known mean-square charge radius $\langle r^2 \rangle_{\text{ch}}$. The matter radius of the proton distribution in nuclei is given by [45]

$$\langle r^2 \rangle_p = \langle r^2 \rangle_{\text{ch}} - \langle r_P^2 \rangle - \langle r_N^2 \rangle N/Z - 0.75/m^2 - \Delta_{\text{ls}}. \tag{36}$$

The values of the charge radii for the proton, $\langle r_P^2 \rangle = 0.7714$, and for the neutron, $\langle r_N^2 \rangle = -0.1149$, were taken from [39]. The last two terms in expression (36) are relativistic corrections, which are usually disregarded (they are about 0.033).

The second term in (35) is usually associated with the square of the halo radius, which is estimated at $R_h = 6.1$ fm in this case.

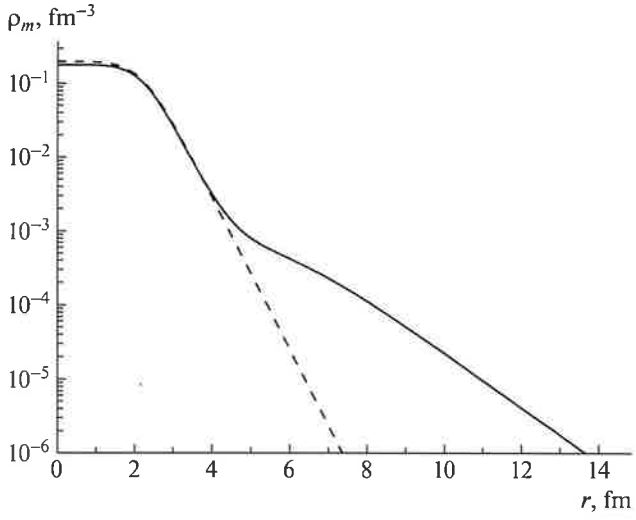

Fig. 8. Matter density of the ^{13}C nucleus: (dashed curve) ground state and (solid curve) $1/2^+$ excited state at 3.09 MeV.

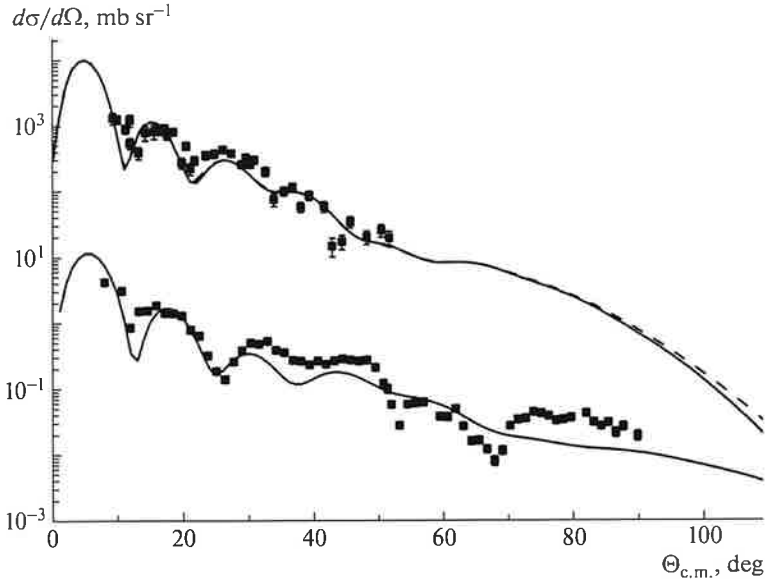

Fig. 9. Differential cross sections for inelastic $\alpha+^{13}C$ scattering at the energies of 65 MeV and 90 MeV (the cross-section values were multiplied by 10^3 in the latter case) that leads to the excitation of the $1/2^+$ state at 3.09 MeV: (points) experimental data, (solid curves) DWBA calculation, and (dashed curve) calculation with an enhanced diffuseness parameter of the imaginary part of the SMDOM potential.

Within the model being considered , the density of the ^{13}C nucleus in the $1/2^+$ state at 3.09 MeV was determined as the sum of the single-particle distribution density of the $2s_{1/2}$ valence neutron and the ground-state density of the ^{12}C nucleus. The latter was calculated within the model of the three-parameter Fermi distribution normalized in a standard way to the number of particles. Use was made of the following parameter values:

$$w_p = w_n = 0.17 \text{ fm}, \quad c_p = c_n = 2.2 \text{ fm}, \quad (37)$$
$$a_p = a_n = 0.39 \text{ fm}.$$

The proton distribution density $\rho_p(r)$ yields a known value for the root-mean-square charge radius, $R_{ch} = 2.47$ fm [39]; the root-mean-square matter radius is $R_m = 2.327$ fm.

For the sake of convenience and in order to improve the accuracy of the computations, this sum was then approximated numerically with a smaller step. The result obtained for the matter density in the $1/2^+$ excited state at 3.09 MeV upon this approximation is shown in Fig. 7 along with the ground-state density.

The distribution of the matter density in the $1/2^+$ excited state at 3.09 MeV is more extended, differing substantially from the ground-state density. In order to render DWBA calculations self-consistent, it is therefore necessary to employ, in calculating the mean-field potential, this excited-state density. An analysis performed anew showed an improved description of the angular distributions at same values of the parameters of the single-particle potential in (34) and somewhat changed values of the normalization factors—$N = 8.6$ at the energy of 65 MeV and $N = 7.0$ at the energy of 90 MeV. The calculated differential cross sections are given in Fig. 8 along with experimental data.

As was indicated by many physicists who studied the scattering of nuclei that have a nucleon halo (see, for example, [46, 47]), the presence of a halo leads to an increase in the absorbing part of the optical potential in the surface region and to the respective dispersion correction to the real part, enlarging the reaction cross section. We have performed a calculation for the case where the diffuseness parameter of the volume part of the dynamical polarization potential was increased by 30%. The result is shown by the dashed line in Fig. 9. The reaction cross section became larger by 10%. The change in the angular distributions turned out to be insignificant in the region where experimental data are available.

4.2.4. Analysis of data on inelastic scattering leading to the excitation of the 8.86-MeV state. This state is viewed as an alpha-cluster state—possibly an analog of the Hoyle state in the ^{12}C nucleus. It has an enhanced root-mean-square matter radius estimated at $R_m = 2.7$ fm (see, for example, [24] and references therein). Available experimental data show a rather strong monopole transition to this state. In order to describe this transition, we considered the inelastic form factor specified by

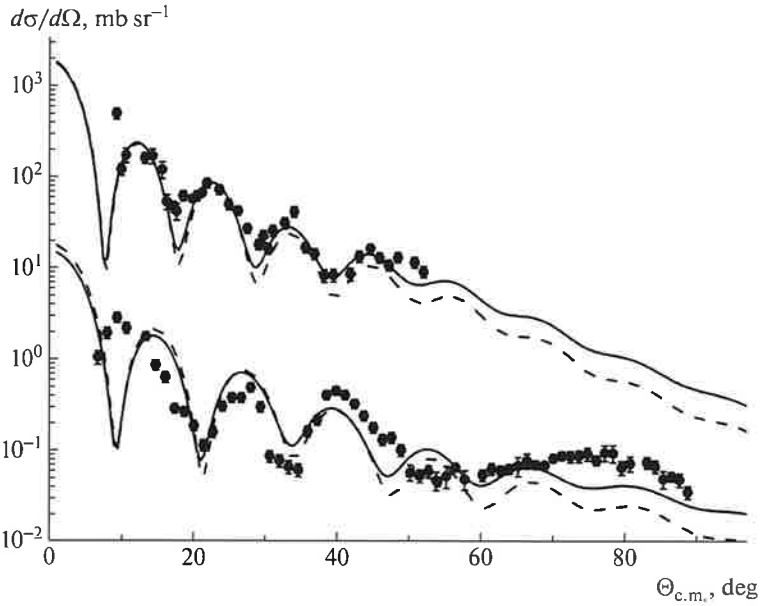

Fig. 10. Differential cross sections for inelastic $\alpha+^{13}$C scattering at the energies of 65 MeV and 90 MeV (the cross-section values were multiplied by 10^3 in the latter case) that leads to the excitation of the $1/2^-$ state at 8.86 MeV: (points) experimental data, (dashed curves) DWBA calculations performed with the ground-state density in the SMDOM potential in the exit channel, and (solid curves) calculations performed with a model density of enhanced radius.

Eqs. (27)–(29), where, for the component $V_L^F(r,E)$ at $L=0$, we took the following simple model expression:

$$V_0^F(r,E) = -\delta_0(4\pi)^{-1/2}d/dr \times \{U_0/[1+\exp((r-R_0)/a_0)]\}. \quad (38)$$

Retaining the condition in (31) for δ_0 and fixing the value of $B(E0, 1/2^- \to 1/2^-) = 0.65e^2$, we determined the parameters δ_0, U_0, R_0, and a_0 from a fit to the shape and normalization of the angular distribution. In just the same way as in preceding case, the analysis of the experimental differential cross sections at the energies of 65 and 90 MeV was first performed by applying, in the exit channel at respective energies, the SMDOM potential (with parameter values from Table 1) involving the mean-field component calculated with the ground-state density of the target nucleus. The results of the calculations are given in Fig. 10 (dashed line) along with experimental data.

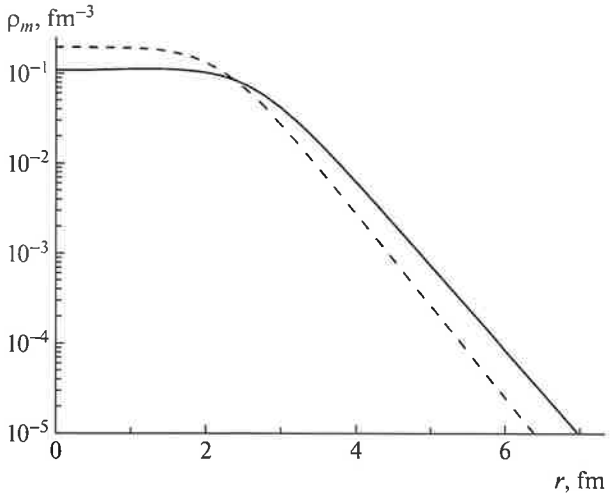

Fig. 11. Matter density of the ^{13}C nucleus: (dashed curve) ground state with $R_m = 2.32$ fm and (solid curve) $1/2^-$ excited state at 8.86 MeV with $R_m = 2.7$ fm.

For the model of the matter density of the ^{13}C nucleus in the $1/2^-$ state at 8.86 MeV, we took a three-parameter Fermi distribution that was normalized in a standard way to the number of particles and whose parameters were chosen in such a way as to obtain the root-mean-square matter radius of 2.7 fm (the radius calculated within the MDM framework is 2.7 ± 0.1 fm [21, 22]); in addition, its shape was required to correspond to the shape of the ground-state distribution approximately to the same extent as the distributions in the ground state and in the Hoyle state of the ^{12}C nucleus correspond to each other—for example, in the AMD model [48]. For the $1/2^-$ state at 8.86 MeV, Fig. 11 shows the model density obtained at the following parameter values:

$$w_p = 0.31 \text{ fm}, \quad c_p = 2.6 \text{ fm}, \quad (39)$$
$$a_p = 0.42 \text{ fm}, \quad w_n = 0.29 \text{ fm},$$

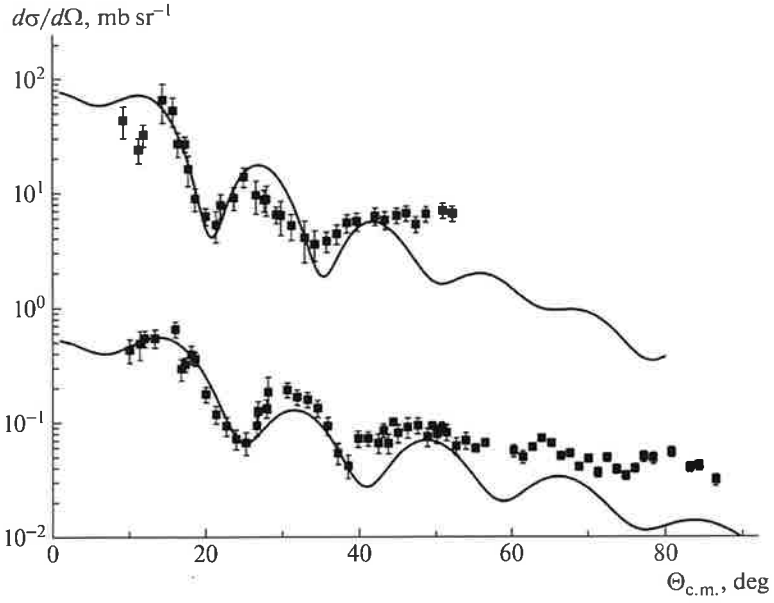

Fig. 12. Differential cross sections for inelastic α+^{13}C scattering at the energies of 65 MeV and 90 MeV (the cross-section values were multiplied by 10^3 in the latter case) that leads to the excitation of the $3/2^-$ state at 9.9 MeV: (points) experimental data and (solid curves) DWBA calculation.

$$c_n = 2.58 \text{ fm}, \quad a_n = 0.42 \text{ fm}.$$

Employing this density, we have calculated anew the mean-field potential, which we used thereupon in the exit-channel potential. This improved somewhat the description of the angular distributions (see Fig. 10) nearly without a change in the parameters of the inelastic form factor that were found earlier [see (37)]

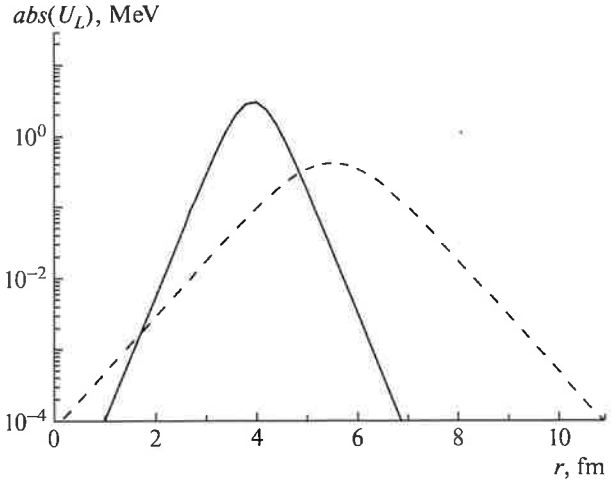

Fig. 13. Form factor for inelastic α+^{13}C scattering occurring at the energy of 90 MeV and leading to the excitation of the (dashed curve) $1/2^-$ state at 8.86 MeV and (solid curve) $3/2^-$ state at 9.9 MeV.

and which became

$$\delta_0 = 0.14 \text{ fm}, \quad U_0 = 22.0 \text{ MeV}, \qquad (40)$$
$$R_0 = 5.514 \text{ fm}, \quad a_0 = 0.55 \text{ fm}.$$

4.2.5. Analysis of data on inelastic scattering leading to the excitation of the 9.9-MeV state. As was indicated in [24], the root-mean-square radius in this state was estimated at $R_m = 2.0\,(0.3)$ fm by means of the MDM analysis. This result is close to the radius of the ^{13}N nucleus in the $3/2^-$ analog state at 9.48 MeV and, within the error interval, complies with the ground-state radius of ^{13}C. In the entrance and exit channels, we therefore used the SMDOM potential containing the mean-field component based on the ground-state density, setting its parameters to the values from Table 1 at respective energies.

Since the nature of this excitation is not clear, we once again made use of the phenomenological inelastic form factor in (27), where, for the component $V_L^F(r,E)$ at $L=2$, we took the model surface form

$$V_2^F(r,E) = -\delta_2(4\pi)^{-1/2} d/dr \qquad (41)$$
$$\times \{U_2/[1+\exp((r-R_2)/a_2)]\}.$$

Retaining the condition in (32) for δ_2 and fixing the value of $B(E2, 1/2^- \to 3/2^-) = 0.22e^2$ fm^4, we determined the parameters δ_2, U_2, R_2, and a_2 from a fit to the shape and normalization of the angular distribution. The results are the following:

$$\delta_2 = 0.22 \text{ fm}, \quad U_2 = 52.0 \text{ MeV}, \qquad (42)$$

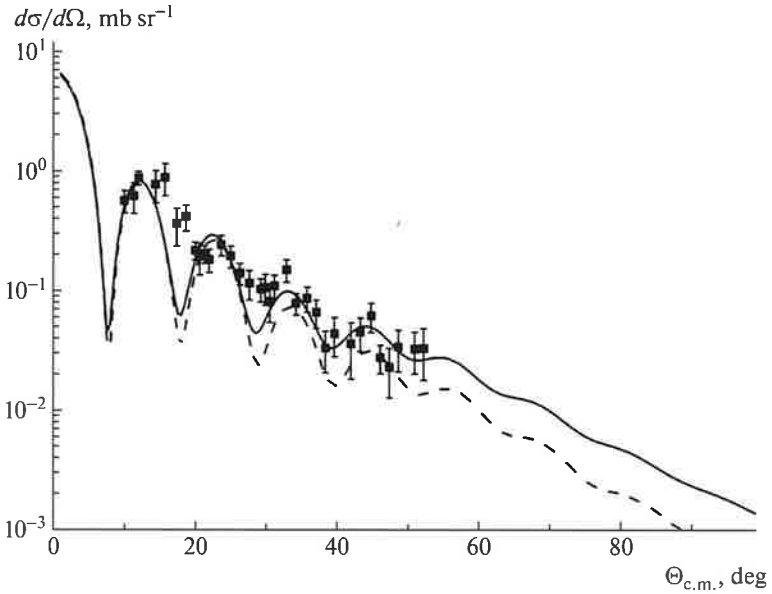

Fig. 14. Differential cross sections for inelastic $\alpha+^{13}$C scattering occurring at the energy of 90 MeV and leading to the excitation of the $1/2^-$ state at 11.08 MeV according to (points) experimental data and DWBA calculations performed by employing (dashed curve) the ground-state density with the SMDOM potential in the exit channel and (solid curve) the model density of enhanced radius.

$$R_2 = 3.939 \text{ fm}, \quad a_2 = 0.25 \text{ fm}.$$

The quality of description of the experimental data is illustrated in Fig. 12.

We note that the inelastic form factor, which is the overlap integral of the ground- and excited-state wave functions, carries information about the nature of the excited state. A comparison of the radial inelastic form factors obtained from our analysis of the transitions to the $1/2^-$ state at 8.86 MeV and the $3/2^-$ state at 9.9 MeV and presented in Fig. 13 shows that the assumption that these states are the first two members of the same rotational band is questionable. More likely, the $3/2^-$ state at 9.9 MeV may itself be the basis of the $K^\pi = 3/2^-$ rotational band.

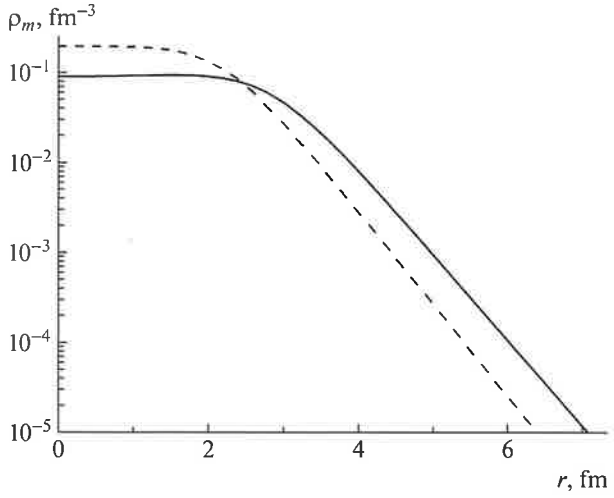

Fig. 15. Material densities of the ^{13}C nucleus in the (dashed curve) ground state with $R_m = 2.32$ fm and (solid curve) $1/2^-$ excited state at 11.08 MeV with $R_m = 2.8$ fm.

Their radial dependence shows that the wave function for the $3/2^-$ state at 9.9 MeV has a substantially smaller spatial extension than the extension of the $1/2^-$ state at 8.86 MeV, and this corresponds to a substantially smaller root-mean-square radius obtained earlier within the MDM framework.

4.2.6. Analysis of data on inelastic scattering leading to the excitation of the 10.996- and 11.08-MeV states. Earlier, it was assumed (see, for example, [24]) that the $1/2^-$ state at 11.08 MeV, as well as the $1/2^-$ state at 8.86 MeV, may be viewed as an alpha-cluster state characterized by an enhanced root-mean-square matter radius estimated at $R_m = 2.8$ fm. Also, experimental data show quite a strong monopole transition to this state.

In order to describe this transition, we therefore employed the same form in (38) for the component $V_L^F(r, E)$ of the inelastic form factor at the fixed value of $B(E0, 1/2^- \to 1/2^-) = 0.056e^2$, determining the parameters δ_0, U_0, R_0, and a_0 from a fit to the shape and normalization of the experimental angular distribution. In just the same way as in the preceding case,

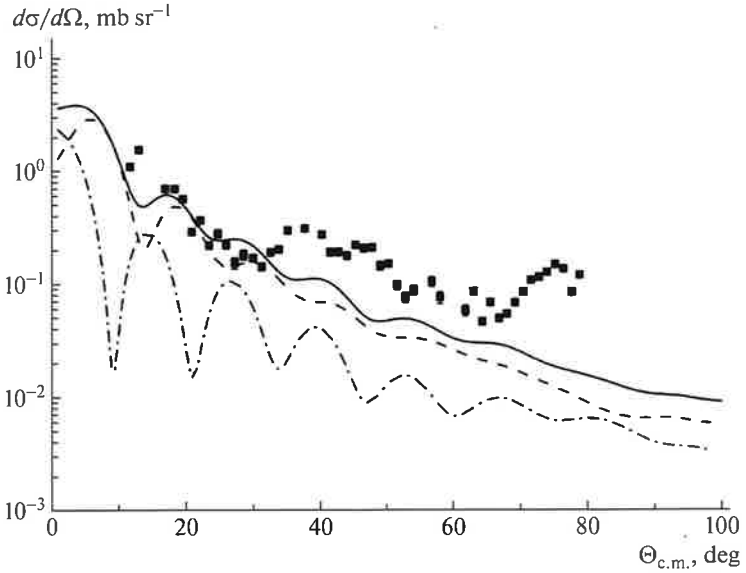

Fig. 16. Differential cross sections for inelastic $\alpha+^{13}C$ scattering at the energy of 65 MeV. The points represent experimental data. The dash-dotted and dashed curves stand for the results of DWBA calculations for the contributions of, respectively, the $1/2^-$ state at 11.08 MeV and the $1/2^+$ state at 10.996 MeV. The solid curve is the sum of these contributions.

we first performed an analysis of the experimental differential cross sections at the energy of 90 MeV, applying, in the exit channel at respective energies, the SMDOM potential whose parameters were set to values in Table 1 and which contains the mean-field component calculated by employing the ground-state density of the target nucleus. The results of respective DWBA calculations are given in Fig. 14 (dashed line) along with relevant experimental data.

For the model of the matter density of the ^{13}C nucleus in the $1/2^-$ state at 11.08 MeV, we then took the three-parameter Fermi distribution normalized in a standard way to the number of particles. The parameters of this distribution were chosen in such a way as to obtain the root-mean-square matter radius of 2.8 fm (the radius calculated within the MDM framework is 2.8 ± 0.2 fm) and to render its shape similar to the shape of the distribution in the $1/2^-$ state at 8.86 MeV. Figure 15 shows the model density obtained for the $1/2^-$ state at 11.08 MeV upon employing the following parameter values:

$$w_p = w_n = 0.3 \text{ fm}, \quad c_p = c_n = 2.8 \text{ fm}, \quad a_p = a_n = 0.42 \text{ fm}. \tag{43}$$

The mean-field potential was calculated anew with this density and was thereupon used in the exit-channel potential.

This improved somewhat the description of the angular distributions (see Fig. 14) nearly without a change in the parameters found earlier for the inelastic form factor:

$$\delta_0 = 0.1 \text{ fm}, \quad U_0 = 20.0 \text{ MeV}, \quad R_0 = 5.514 \text{ fm}, \quad a_0 = 0.60 \text{ fm}. \tag{44}$$

After that, we analyzed the data at the energy of 65 MeV. Unfortunately, the $1/2^-$ state at 11.08 MeV and the $1/2^+$ state at 10.996 MeV were not separated experimentally in that case. Therefore, we had to consider the summed contribution of the angular distributions of these states. For the $1/2^-$ state at 11.08 MeV, we took the same form factor as that at the energy of 90 MeV, only changing the value of the normalization parameter δ_0. The second state has a very close excitation energy; therefore, it is natural to assume that is also a cluster state characterized by an enhanced radius that is close to the radius of the $1/2^-$ state at 11.08 MeV. For the inelastic transition occurring to the $1/2^+$ state at 10.996 MeV with orbital-angular-momentum transfer $L = 1$, we used the same model expression (27) for the form factor with the component $V_L^F(r, E)$ of the inelastic form factor; that is,

$$V_1^F(r, E) = -\delta_1 (4\pi)^{-1/2} d/dr \times \{U_1/[1 + \exp((r - R_1)/a_1)]\}. \tag{45}$$

At the fixed value of $B(E1, 1/2^- \to 1/2^+) = 0.018e^2$ fm^2, the parameters δ_1, U_1, R_1, a_1, and δ_0 were determined from a fit to the shape and normalization of the summed angular distribution.

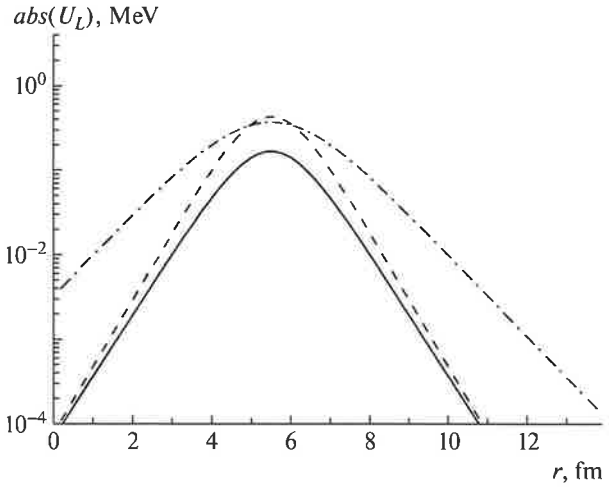

Fig. 17. Form factor for inelastic $\alpha+^{13}C$ scattering occurring at the energy of 90 MeV and leading to the excitation of the (dashed curve) $1/2^-$ state at 8.86 MeV, (solid curve) $1/2^-$ state at 11.08 MeV, and (dash-dotted curve) $1/2^+$ state at 10.996 MeV.

In the entrance and exit channels, we used the SMDOM optical potentials at respective energies with parameters set to the values in Table 1 and with allowance for the enhanced radii of the density in calculating the mean-field component. The quality of description of experimental data is illustrated in Fig. 16.

We have obtained the following parameter values:

$$\delta_0 = 0.07\ \text{fm}, \quad \delta_1 = 0.3\ \text{fm}, \quad (46)$$
$$U_1 = 15.5\ \text{MeV}, \quad R_1 = 5.514\ \text{fm},$$
$$a_1 = 0.9\ \text{fm}.$$

Figure 17 shows the components $V_L^F(r, E)$ of the inelastic form factors for the $1/2^-$ state at 11.08 MeV, the $1/2^+$ state at 10.996 MeV, and the $1/2^-$ state at 8.86 MeV.

On the basis of the component determined for the 10.996-MeV state, the radius of this state was estimated for the first time within the MDM framework. The result is 2.9 ± 0.1 fm.

A comparison of the shapes of the inelastic form factors that we obtained gives ground to assume that, in all three states, the ^{13}C nucleus, has enhanced radii and similar structures.

5. CONCLUSIONS

A theoretical analysis of experimental data on elastic and inelastic alpha-particle scattering on ^{13}C nuclei at the energies of 65 and 90 MeV that leads, in the case of inelastic scattering, to the excitation of the states at 3.09, 3.68, 7.55, 8.86, 9.90, and 11.08 MeV have been performed. Data on the angular distributions for the states at 3.68 and 7.55 MeV have been presented for the first time.

Data on elastic scattering in the energy range of $E_{\text{lab}} = 48.7$–90 MeV were analyzed on the basis of the SemiMicroscopic Dispersive Optical Model (SMDOM). This model, which resorts to dispersion relations, effectively involves a smaller number of variable parameters than the usual phenomenological optical model, where one determines the whole set of parameters at each energy value individually. This makes it possible to reduce the ambiguity of the analysis. Within this approach, the mean-field potential has been calculated microscopically on the basis of the double-folding model with allowance for the exchange component. In particular, the empirical energy dependence of the volume integral has been found for the mean-field potential. The parameters of the SMDOM potential have been determined. The use of rainbow effects observed in differential cross sections also made it possible to reduce the ambiguity in determining the parameters of the optical potential, and a smooth energy dependence of the parameters of the constructed potential in the energy range being considered permitted estimating the parameters and integrated characteristics of the potential at energies of exit inelastic-scattering channel. A rather good description of the data on elastic scattering has been obtained.

Experimental data on inelastic scattering have been analyzed with the aid of the DWBA method. In this analysis, we have employed the strength parameters of the SMDOM potential at the respective energies that was obtained above.

Data on the states at 3.68 and 7.55 MeV have been analyzed under the assumption that these states are members of the ground-state rotational band. The data have been well described in the region of first diffraction oscillations, whereby the validity of this assumption is confirmed. Within the MDM framework, we have obtained, for these states, radii that, within the errors, agree with the ground-state radius. These two results confirm that the band in question may indeed exist.

The $1/2^+$ state at 3.09 MeV has been treated as a single-particle excitation of the valence neutron in the s state in the potential of the ^{12}C core in the ground state. The radial form factor is determined by the overlap integral of the nucleon–nucleon interaction and the single-particle wave functions for the $1p_{1/2}$ valence neutron in the ground state of the ^{13}C target nucleus and the $2s_{1/2}$ valence neutron in the $1/2^+$ exited state of the ^{13}C nucleus at 3.09 MeV. The single-particle wave function obtained for the $2s_{1/2}$

valence neutron has a large extension (its root-mean-square radius is $R_n = 6.36$ fm), showing signatures of a neutron halo in the ^{13}C nucleus in the $1/2^+$ excited state at 3.09 MeV. The estimation of the root-mean-square radius of the ^{13}C nucleus (R_m) in this state on the basis of the model being considered yields $R_m = 2.8$ fm. A similar value of the radius was also obtained within the MDM framework, 2.9 ± 0.2 fm. The distribution of the matter density in this state turned out to be more extended, differing substantially from the ground-state density. In order to render the DWBA calculation self-consistent, it is therefore necessary to employ, in calculating the mean-field potential in the exit channel, this excited-state density. The use of this rarefied density improved the description of experimental data. In summary, these data are rather well described over the whole energy range.

Our analysis has made it possible to extract the component corresponding to the 10.996-MeV state and to estimate for the first time the radius of this state within the MDM framework. The states at 8.86, 10.996, and 11.08 MeV have been treated as alpha-cluster states. The data in question are rather well described over the whole energy range. Moreover, the form factors obtained for these states behave similarly, which is indicative of the proximity of their properties. It turns out that, within the errors, the radii of these states agree with one another and that they are close to the radius of the Hoyle state. These results support the assumption that the alpha-cluster states in question are analogs of the Hoyle state in ^{12}C.

For the 9.90 MeV state, we have employed a fully phenomenological inelastic form factor since the nature of this excitation is not clear. Owing to this, we were able to attain a good description of the experimental data in the region of first diffraction oscillations. A comparison of the form factor obtained for this state with the form factor for the state at 8.86 MeV demonstrates strongly different types of behavior and a smaller spatial extension for the state at 9.90 MeV. This confirms once again the reduced radius that we obtained within the MDM framework.

The analysis that we performed by applying the DWBA method has confirmed our results obtained earlier from MDM calculations. Once again, the coexistence of different structures in ^{13}C have been demonstrated. Specifically, shell states neighbor collective rotational states and exotic structures, such as a neutron halo and alpha-cluster states characterized by enhances radii. The problem of the compact state at 9.90 MeV remains open and will possible require a new experiment with a ^{3}He beam.

Our present analysis has confirmed once again the potential of the distorted-wave method, which may provide information about the wave function for the state of interest via tests of various nuclear models in terms of the reaction form factor, which is the overlap integral of the wave functions for the primary target nucleus and the final nuclear product in the state being studied. Moreover, such a theoretical analysis permits separating, in the cases where this is impossible in experimental data, the contributions of close levels or the contributions of several components associated with different angular-momentum transfers. This was successfully done for the experimental data at 65 MeV: the components of the states at 3.68 and 3.85 MeV, as well as the components of the states at 10.996 and 11.08 MeV, could be singled out in the common peak.

FUNDING

The reported study was funded by the NRC Kurchatov Institute.

REFERENCES

1. W. von Oertzen, M. Freer, and Y. Kanada-En'yo, Phys. Rep. **432**, 43 (2006).
2. A.Tohsaki, H. Horiuchi, P. Schuck, and G. Röpke, Phys. Rev. Lett. **87**, 192501 (2001).
3. P. Schuck, Y. Funaki, H. Horiuchi, G. Röpke, A. Tohsaki, and T. Yamada, Nucl. Phys. A **738**, 94 (2004).
4. M. Chernykh, H. Feldmeier, T. Neff, P. von Neumann-Cosel, and A. Richter, Phys. Rev. Lett. **98**, 032501 (2007).
5. A. A. Ogloblin, T. L. Belyaeva, A. N. Danilov, A. S. Demyanova, and S. A. Goncharov, Nucl. Phys. A **834**, 143 (2010).
6. T. L. Belyaeva, A. N. Danilov, A. S. Demyanova, S. A. Goncharov, A. A. Ogloblin, and R. Perez-Torres, Phys. Rev. C **82**, 054618 (2010).
7. T. Kawabata, Y. Sasamoto, M. Fujiwara, H. Hashimoto, K. Hatanaka, K. Itoh, M. Itoh, Y. Kanada-En'yo, K. Kawase, Y. Maeda, H. Matsubara, K. Nakanishi, S. Sakaguchi, Y. Shimizu, K. Suda, Y. Tameshige, et al., J. Phys.: Conf. Ser. **111**, 012013 (2008).
8. T. Kawabata, Y. Sasamoto, Y. Maeda, S. Sakaguchi, Y. Shimizu, K. Suda, T. Uesaka, M. Fujiwara, H. Hashimoto, K. Hatanaka, K. Kawase, H. Matsubara, K. Nakanishi, Y. Tameshige, A. Tamii, K. Itoh, et al., Int. J. Mod. Phys. E **17**, 2071 (2008).
9. T. Yamada and Y. Funaki, Int. J. Mod. Phys. E **17**, 2101 (2008).
10. T. Yamada and Y. Funaki, Int. J. Mod. Phys. E **20**, 910 (2011).
11. T. Yamada and Y. Funaki, Phys. Rev. C **92**, 034326 (2015).
12. Y. Chiba and M. Kimura, Phys. Rev. C **101**, 024317 (2020).
13. M. Milin and W. von Oertzen, Eur. Phys. J. A **14**, 295 (2002).
14. N. Furutachi and M. Kimura, Phys. Rev. C **83**, 021303(R) (2011).

15. N. Itagaki, W. von Oertzen, and S. Okabe, Phys. Rev. C **74**, 067304 (2006).
16. T. Otsuka, N. Fukunishi, and H. Sagawa, Phys. Rev. Lett. **70**, 1385 (1993).
17. Z. H. Liu, C. J. Lin, H. Q. Zhang, Z. C. Li, J. S. Zhang, Y. W. Wu, F. Yang, M. Ruan, J. C. Liu, S. Y. Li, and Z. H. Peng, Phys. Rev. C **64**, 034312 (2001).
18. T. L. Belyaeva, R. Perez-Torres, A. A. Ogloblin, A. S. Demyanova, S. N. Ershov, and S. A. Goncharov, Phys. Rev. C **90**, 064610 (2014).
19. A. N. Danilov, T. L. Belyaeva, A. S. Demyanova, S. A. Goncharov, and A. A. Ogloblin, Phys. Rev. C **80**, 054603 (2009).
20. A. S. Demyanova et al., Int. J. Mod. Phys. E **20**, 915 (2011).
21. A. S. Demyanova, A. N. Danilov, S. V. Dmitriev, A. A. Ogloblin, T. L. Belyaeva, N. Burtebaev, P. Drobyshev, S. A. Goncharov, Yu. B. Gurov, P. Heikkinen, R. Julin, S. V. Khlebnikov, V. A. Maslov, N. Nassurlla, Yu. E. Penionzhkevich, Yu. G. Sobolev, et al., EPJ Web Conf. **66**, 02027 (2014).
22. A. S. Demyanova, A. A. Ogloblin, A. N. Danilov, S. A. Goncharov, T. L. Belyaeva, Yu. G. Sobolev, S. V. Khlebnikov, N. Burtebaev, W. Trzaska, P. Heikkinen, G. P. Tyurin, D. Janseitov, and Yu. B. Gurov, EPJ Web Conf. **117**, 04012 (2016).
23. A. A. Ogloblin, A. S. Demyanova, A. N. Danilov, S. A. Goncharov, T. L. Belyaeva, V. Trzaska, and Yu. G. Sobolev, JETP Lett. **102**, 199 (2015).
24. A. S. Demyanova, A. N. Danilov, S. V. Dmitriev, A. A. Ogloblin, V. I. Starastsin, S. A. Goncharov, and D. M. Janseitov, JETP Lett. **114**, 303 (2021).
25. B. A. Urazbekov, B. K. Karakozov, N. T. Burtebayev, D. M. Janseitov, M. Nasrulla, D. Alimov, D. S. Valiolda, S. H. Kazhykenov, A. S. Denikin, A. S. Demyanova, and A. N. Danilov, Int. J. Mod. Phys. E **31**, 2250031 (2022).
26. D. J. Marín-Lámbarri, R. Bijker, M. Freer, M. Gai, Tz. Kokalova, D. J. Parker, and C. Wheldon, Phys. Rev. Lett. **113**, 012502 (2014).
27. R. Bijker and F. Iachello, Phys. Rev. Lett. **122**, 162501 (2019).
28. I. J. Thompson, Comput. Phys. Rep. **7**, 167 (1988).
29. P. D. Kunz and E. Rost, Comput. Nucl. Phys. **2**, 88 (1993).
30. S. A. Goncharov, O. M. Knyaz'kov, and A. A. Kolozhvari, Phys. At. Nucl. **59**, 634 (1996).
31. G. R. Satchler, *Direct Nuclear Reactions* (Clarendon, Oxford, 1983).
32. D. T. Khoa and G. R. Satchler, Nucl. Phys. A **668**, 3 (2000).
33. S. A. Goncharov and A. Izadpanakh, Phys. At. Nucl. **70**, 18 (2007).
34. S. A. Goncharov and A. Izadpanakh, Phys. At. Nucl. **70**, 1491 (2007).
35. S. A. Goncharov and R. V. Sukhorukov, Mosc. Univ. Phys. Bull. **73**, 301 (2018).
36. D. T. Khoa, G. R. Satchler, and W. von Oertzen, Phys. Rev. C **56**, 954 (1997).
37. M. W. Kirson, Nucl. Phys. A **781**, 350 (2007).
38. J. Heisenberg, J. S. McCarthy, and I. Sick, Nucl. Phys. A **157**, 435 (1970).
39. I. Angeli and K. P. Marinova, At. Data Nucl. Data Tables **99**, 69 (2013).
40. S. A. Goncharov, Yu. A. Glukhov, A. S. Demyanova, A. A. Oglobin, M. V. Rozhkov, and V. Trashka, Izv. Akad. Nauk, Ser. Fiz. **67**, 72 (2003).
41. H. Abele, H. J. Hauser, A. Korber, W. Leitner, R. Neu, H. Plappert, T. Rohwer, G. Staudt, M. Strasser, S. Welte, M. Walz, P. D. Eversheim, and F. Hinterberger, Z. Phys. A **326**, 373 (1987).
42. A. Ingemarsson, J. Nyberg, P. U. Renberg, O. Sundberg, R. F. Carlson, A. J. Cox, A. Auce, R. Johansson, G. Tibell, D. T. Khoa, and R. E. Warner, Nucl. Phys. A **676**, 3 (2000).
43. C. Mahaux, H. Ngo, and G. R. Satchler, Nucl. Phys. A **449**, 354 (1986).
44. H. T. Fortune, Phys. Rev. C **94**, 064307 (2016).
45. J. L. Friarand and J. W. Negele, Adv. Nucl. Phys. **8**, 219 (1975).
46. G. R. Satchler, K. W. Mcvoy, and M. S. Hussein, Nucl. Phys. A **522**, 621 (1991).
47. S. A. Goncharov and A. A. Ogloblin, Phys. At. Nucl. **56**, 40 (1993).
48. Y. Kanada-En'yo, Prog. Theor. Phys. **117**, 655 (2007).